AGU PUBLICATIONS

JGR

Journal of Geophysical Research: Atmospheres

RESEARCH ARTICLE
10.1002/2016JD026075

Key Points:
- SAH movements and area changes have different influences on extreme precipitation over the eastern China
- SAH movements influence extreme precipitation through the propagation of Rossby wave train
- SAH area changes influence the extreme precipitation through the western Pacific subtropical High

Correspondence to:
J. Liu,
jliu@njnu.edu.cn

Citation:
Ning, L., J. Liu, and B. Wang (2017), How does the South Asian High influence extreme precipitation over eastern China?, *J. Geophys. Res. Atmos.*, *122*, 4281–4298, doi:10.1002/2016JD026075.

Received 11 OCT 2016
Accepted 13 MAR 2017
Accepted article online 17 MAR 2017
Published online 27 APR 2017

How does the South Asian High influence extreme precipitation over eastern China?

Liang Ning[1,2,3], Jian Liu[1,2], and Bin Wang[4,5]

[1]Key Laboratory of Virtual Geographic Environment, Ministry of Education, State Key Laboratory of Geographical Environment Evolution, Jiangsu Provincial Cultivation Base, School of Geography Science, Nanjing Normal University, Nanjing, China, [2]Jiangsu Center for Collaborative Innovation in Geographical Information Resource Development and Application, Nanjing, China, [3]Climate System Research Center, Department of Geosciences, University of Massachusetts Amherst, Amherst, Massachusetts, USA, [4]Department of Atmospheric Sciences, International Pacific Research Center, University of Hawai'i at Mānoa, Honolulu, Hawaii, USA, [5]Earth System Modeling Center, Nanjing University of Information Science and Technology, Nanjing, China

Abstract Based on the high-resolution observed daily precipitation data, three characteristic regions over eastern China are first defined through the rotated empirical orthogonal function. Then, the relationship between summer (June-July-August) extreme precipitation across the three characteristic regions of eastern China and the South Asian High (SAH) is examined to determine how the northwest-southeast movement and area (magnitude) of SAH influence the summer extreme precipitation across eastern China. When the South Asian High is located anomalously northwest, there is more extreme precipitation over the northern part of eastern China but less extreme precipitation over the Jiang-Huai River Basin. When the SAH intensifies, there is more extreme precipitation over the Jiang-Huai River Basin. The mechanisms are that under the conditions of anomalously northwestward displacements, the positive geopotential anomalies over central Asia induce a deep barotropic Korean High through a Rossby wave train, resulting in more water vapor transportation to eastern China with more convergence over the northern part of eastern China located at the northwestern edge of the Korean High but with a divergence over the Jiang-Huai River Basin. When the SAH intensifies, accompanied by an enhanced and westward extended western Pacific subtropical High, the convergence over the Jiang-Huai River Basin increases with enhanced water vapor transportation due to the confluence of warm and cold advections. These mechanisms are achieved through shifts toward the high tail (low tail) of the daily precipitation cumulative distributions of these two regions and finally increases (decreases) in the occurrence of extreme precipitation.

1. Introduction

Because of the large impacts on the society and ecosystems, climate extremes have attracted increasing attention in recent climate studies [*Easterling et al.*, 2000a, 2000b; *Meehl and Tebaldi*, 2004; *Li et al.*, 2013; *Coffel and Horton*, 2015]. The Intergovernmental Panel on Climate Change Fifth Assessment Report indicates that the globally averaged surface air temperature shows a warming of 0.85°C over the period of 1880–2012, with significant increases in different climate extremes over different regions [*Frich et al.*, 2002; *Alexander et al.*, 2006; *Hartmann et al.*, 2013; *Donat et al.*, 2013; *Sillmann et al.*, 2013a]. Since these increases will probably continue under the background of future warming [*Meehl et al.*, 2007; *Sillmann et al.*, 2013b; *Horton et al.*, 2015; *Ning et al.*, 2015], a better understanding on the mechanisms influencing regional climate extremes is needed to improve the predictions of future climate extremes.

To analyze the mechanisms behind the variations of regional climate extremes, one major aspect is to investigate the influences from prominent large-scale circulation modes, such as the North Atlantic Oscillation [*Wallace and Gutzler*, 1981; *Barnston and Livezey*, 1987], Pacific-North American pattern (PNA) [*Wallace and Gutzler*, 1981; *Leathers et al.*, 1991], and El Niño–Southern Oscillation (ENSO) [*Trenberth*, 1997]. Previous studies have revealed that both the regional mean climate [e.g., *Rasmusson and Wallace*, 1983; *Ropelewski and Halpert*, 1986; *Hartley and Keables*, 1998; *Kunkel and Angel*, 1999; *Bradbury et al.*, 2003; *Ning et al.*, 2012a, 2012b; *Ning and Bradley*, 2014, 2016] and climate extremes [e.g., *Wettestein and Mearns*, 2002; *Brown et al.*, 2008; *Loikith and Broccoli*, 2014a, 2014b; *Ning and Bradley*, 2015a] are influenced by these large-scale circulation modes. For example, *Griffths and Bradley* [2007]observed increases in both

temperature and precipitation extremes in 1926–2000 in the northeast U.S., and some of the variability associated with changes in these extremes can be explained by variations in the Arctic Oscillation (AO), ENSO, and PNA. *Ning and Bradley* [2015b] indicated that two types of El Niño, i.e., the eastern Pacific El Niño and central Pacific El Niño [*Yu et al*., 2012; *Liang et al*., 2014], have significantly different influences on winter climate extremes over the eastern U.S. because of the different circulation anomalies resulting from different wave train patterns at the 500 hPa level. Over eastern China, the AO and ENSO were found to be related to the winter extreme warm and cold days through the application of the generalized extreme value distribution theory [*Chen et al*., 2013]. When examining the relationship of the ENSO and the frequency of extreme precipitation events in China, *Li et al*. [2011] found that during winter and spring, extreme precipitation events occur more often during El Niño events than during La Niña events, while the opposite was found during summer and autumn. *Mao et al*. [2011] also showed that a positive AO usually induces significant winter extreme precipitation over central southern China through a stronger Middle East jet stream and deepened southern branch trough over the Bay of Bengal.

Eastern China is located in the East Asian summer monsoon (EASM), and the summer (June-July-August) precipitation over eastern China is directly influenced by the EASM. Usually, a stronger EASM corresponds to more precipitation over northern China, whereas a weaker EASM leads to more precipitation over the Yangtze-Huai River valley [*Zhang*, 2015]. Therefore, the summer precipitation over eastern China can be used to reflect the intensity of the EASM [*Wang et al*., 2008]. The EASM is also influenced by other circulation systems, such as the western Pacific subtropical high (WPSH) [*Wang et al*., 2013]. *Zhou et al*. [2009] found that the westward extension of the WPSH is a possible reason for changes in the EASM and summer precipitation in the late 1970s when the EASM weakened and more rainfall occurred over the lower reach of the Yangtze River valley. In addition to the EASM and WPSH, another large-scale circulation pattern exerting significant influence the summer precipitation over eastern China is the Silk Road pattern [*Enomoto et al*., 2003]. This pattern is a propagation of a Rossby wave train along the Asian jet in the upper troposphere over the Eurasia continent, and it was found to significantly impact precipitation over North China and the Yangtze River valley [*Chen and Huang*, 2012; *Zhang and Zhou*, 2015].*Huang et al*. [2013] also indicated that the interdecadal change of summer precipitation over eastern China during the late 1990s was induced by the weakening and poleward shift of the East Asia subtropical westerly jet through the changes of the Silk Road pattern over the Eurasia continent. These three systems also show combined effects on the summer precipitation over eastern China. For example, *Wang and He* [2015] demonstrated that the intensified Silk Road pattern was responsible for the strongly positive precipitation anomaly over the Yangtze River valley and negative precipitation anomaly over northeastern China in 2014 through a southward shift of the WPSH and a weakening of the EASM.

Eastern China has a large human population and encompasses an enormous diversity of geography, climate, ecological resources, and human land use. During the last several decades, eastern China has experienced significantly increasing trend in extreme precipitation events [*Zhai et al*., 1999; *Ren et al*., 2000]. These increases have brought large influences to the regional society and economy. Consequently, eastern China poses many unique challenges for understanding, adapting to and mitigating the effects of extreme precipitation. Previous studies have shown that the modes of large-scale circulations, such as the ENSO, can cause different impacts to the amount and frequency of extreme precipitation over eastern China [e.g., *Li et al*., 2011]. These increases in extreme precipitation during recent decades have also been found to be potentially caused by the trends of circulation over East Asia, e.g., the strengthening trend of the continental high over Eurasia and the weakening trend of the western Pacific subtropical High [*Wang and Zhou*, 2005]. *Ning and Qian* [2009] also indicated that the significant increase of summer extreme precipitation events over south China during the early 1990s were caused by the interdecadal variations of the latent heat over the South China Sea and sensible heat over Indochina. When investigating the variations of extreme precipitation over China, *Wang et al*. [2014] found that the annual extreme precipitation was associated with the sea surface temperature around the Indian Ocean and the South and East China Seas. *You et al*. [2011] also demonstrated that the decline of the Asian monsoon circulation strength has contribution to severe rainfall anomalies including floods in southern China and droughts in the north over recent decades.

In addition to the above circulation patterns, the South Asian High (SAH), which is an important semipermanent anticyclonic circulation pattern in the upper troposphere over the Asian continent in the boreal summer [*Mason and Anderson*, 1958], also shows strong influences on the different aspects of climate over Asia and

China, such as the Asian summer monsoon onset and rainfall [*Liu et al*., 2013; *Wei et al*., 2014] and the summer rainfall variation overall of China [*Wei et al*., 2015]. Previous studies suggested that the SAH is a regulator of the EASM [*Zhang et al*., 2016]. A strong and eastward expanding upstream SAH is ordinarily accompanied by a downstream intensified WPSH stretching westward and a correspondingly weaker EASM, resulting in positive precipitation anomalies over the Yangtze River Valley [*Jiang et al*., 2011]. While most of the previous studies of the SAH mainly focused on the seasonal mean climate, in this study, we investigate how the low-frequency SAH influences the summer extreme precipitation events defined on daily scale over eastern China and the corresponding mechanisms. Moreover, since the location and magnitude of the SAH can be predicted in advance [*Qian et al*., 2002], these findings can be helpful to improve the seasonal prediction of extreme precipitation over eastern China. This analysis improves our understanding of the dynamics of extreme precipitation over eastern China and helps reduce the uncertainties of predictions of regional climate extremes, which are highly relevant to a wide range of interdisciplinary interests, such as regional water resources, ecosystems, and the environment.

2. Data and Methodology

2.1. Data

The study area covers the mainland area of China (15°–55°N, 70°–140°E). The high-resolution (0.25° × 0.25°) observed daily precipitation data for the period of 1961–2014 from the China Meteorological Administration, known as the CN05.1 data set, were used in this study. As previously conducted by *Xu et al*. [2009], the CN05.1 data set was constructed from an interpolation (using the "anomaly approach") of 2416 observation stations in China with quality control [*Wu and Gao*, 2013]. In the anomaly approach, a gridded climatology is first calculated, and then a gridded daily anomaly is added to the climatology to obtain the final data set.

In the mechanism analysis section, the monthly gridded 1000 hPa to 500 hPa geopotential height, *u* and *v* components of the wind, specific humidity, and omega data with a resolution of 2.5° × 2.5° for the period of 1961–2014 were from the National Center for Environmental Prediction (NCEP) reanalysis data [*Kalnay et al*., 1996]. Among the circulation variables, the vertically integrated low-level average moisture flux components were calculated using the following equations [*Coleman and Rogers*, 2003; *Dominguez and Kumar*, 2005]:

$$qu = \frac{1}{g}\int_{1000\mathrm{hPa}}^{500\mathrm{hPa}} \overline{q}\,\bar{u}\,\mathrm{d}p, \tag{1}$$

$$qv = \frac{1}{g}\int_{1000\mathrm{hPa}}^{500\mathrm{hPa}} \overline{q}\,\bar{v}\,\mathrm{d}p, \tag{2}$$

where *qu* and *qv* are the zonal and meridional moisture flux components and $\overline{q}$, $\bar{u}$, and $\bar{v}$ are the seasonal mean specific humidity and the zonal and meridional wind components at each pressure level. The two-dimensional moisture flux field was calculated by

$$\mathbf{q} = qu\mathbf{i} + qv\mathbf{j}, \tag{3}$$

where the **q** is the low-level horizontal moisture flux and **i** and **j** are the unit zonal and meridional vectors.

2.2. Definition of Extreme Precipitation

The definition of a summer extreme precipitation event is taken from the dictionary of the European Climate Assessment and Dataset as a daily precipitation larger than the 95th percentile of the summer daily precipitation amount. This definition has been commonly used in previous studies of extreme precipitation [e.g., *Frich et al*., 2002; *Meehl and Tebaldi*, 2004; *Alexander et al*., 2006; *Ning & Bradley*, 2015a, 2015b]. The summer extreme precipitation is represented by the following two indices: total number of extreme precipitation events and total amount of extreme precipitation over the entire season. The total number of extreme precipitation events is defined as the total number of days with precipitation above the threshold. The summer extreme precipitation contributes to approximately 40%–70% of the total summer rainfall over eastern China [*Wang and Zhou*, 2005].

2.3. Rotated Empirical Orthogonal Function

Empirical orthogonal function (EOF) analysis is a widely used statistical technique to reduce a complex data set into linear combinations of fewer new variables [*Wilks*, 2006]; therefore, EOF analyses have been extensively used to characterize the dominant spatial patterns and the corresponding temporal variability of three-dimensional data sets in atmospheric research [e.g., *Joyce*, 2002; *Ning and Bradley*, 2014]. Although the orthogonality of EOF analysis has the great advantage of isolating principal patterns from complex data, it can also induce artificial structures and difficulty in physical interpretations [*Hannachi*, 2007]. Thus, the rotated EOF (REOF) analysis was introduced to alleviate these problems of traditional EOF analysis [*Lian and Chen*, 2012]. The major advantage of REOF is that REOF linearly transforms the spatial patterns derived by EOF analysis into a rotated basis based on the variance and updates the alignment of the eigenfunctions with the actual data so that it can improve the description of the relationship between their spatiotemporal patterns and physical mechanisms [*Lian and Chen*, 2012]. Previous studies have shown that REOF analysis can avoid the unphysical dipole-like patterns generated from traditional EOF analysis [*Dommenget and Latif*, 2002].

2.4. Definitions of SAH Indices

Figure 1 shows the summer climatological 200 hPa geopotential height field for the period of 1961–2014, and the SAH is the major circulation feature over the subtropical region of the Northern Hemisphere with its center located at (22.5–32.5°N, 50–100°E). Previous studies have found that the SAH has the following four characteristics: zonal variation (i.e., bimodality) [*Zhang et al*., 2002], meridional variation [*Wei et al*., 2012], intensity variation, and extension variation [*Zhang and Qian*, 2000]. To quantitatively depict the variability of locations and magnitudes of SAH, four SAH indices have been calculated herein following the previous studies [*Zhang and Qian*, 2000; *Wei et al*., 2012], i.e., the north-south shift index, the west-east shift index, the area index, and the magnitude index. The north-south shift index (SAHI-NS) is defined as the difference of regional averaged geopotential height between the northern part (27.5–32.5°N, 50–100°E) and the southern part (22.5–27.5°N, 50–100°E) of the SAH center (Figure 2a). The west-east shift index (SAHI-WE) is defined as the difference of regional averaged geopotential height between the western part (22.5–32.5°N, 50–75°E) and the eastern part (22.5–32.5°N, 75–100°E) of the SAH center (Figure 1b). The area index (SAHI-area) is defined as the number of grid points within the isoline of 12,500 geopotential meters (gpm) that was thickened in Figure 1. The magnitude index (SAHI-mag) is defined as the averaged magnitude of grid points within the isoline of 12,500 gpm.

The correlations among the four indices are given in Table 1. From the table, it can be concluded that the SAHI-NS and SAHI-WE are significantly correlated with each other ($p < 0.05$), indicating that when the SAH shifts to the north, it may also shift to the west, but they are not correlated with the SAHI-area or SAHI-mag. Thus, we have combined the SAHI-NS and SAHI-WE together through defining a new index, SAHI-NW, as the difference of regional averaged geopotential height between the northwestern part (27.5–32.5°N, 50–75°E) and the southeastern part (22.5–27.5°N, 75–100°E) of the SAH center. The SAHI-area and SAHI-mag are highly correlated with each other ($r = 0.95$), indicating that when SAH intensifies, it also extends to a larger area. Therefore, in the following analysis, the results based on SAHI-mag are not shown since they are almost the same as the results based on SAHI-area.

3. Results

3.1. Characteristics of Summer Extreme Precipitation Over Eastern China

In this study, REOF analysis was first applied to the total amount of summer extreme precipitation over eastern China with the linear trend removed, and the first 10 principal components of the original EOF analysis with the covariance matrix were retained during the rotation. The first three REOF patterns explain nearly 25% of the total variance. This percentage is low but still reasonable considering the explained variance in the EOF analysis applied to precipitation is typically low due to the nonlinear component of the precipitation variance [e.g., *Joyce*, 2002; *Wu et al*., 2005; *Ge et al*., 2009] and the fact that extreme precipitation has even stronger nonlinear characteristics. When applying North's rule of thumb [*Wilks*, 2006; *Hannachi et al*., 2007], the first two modes can be statistically separable, so the following discussion mainly focuses on these two modes.

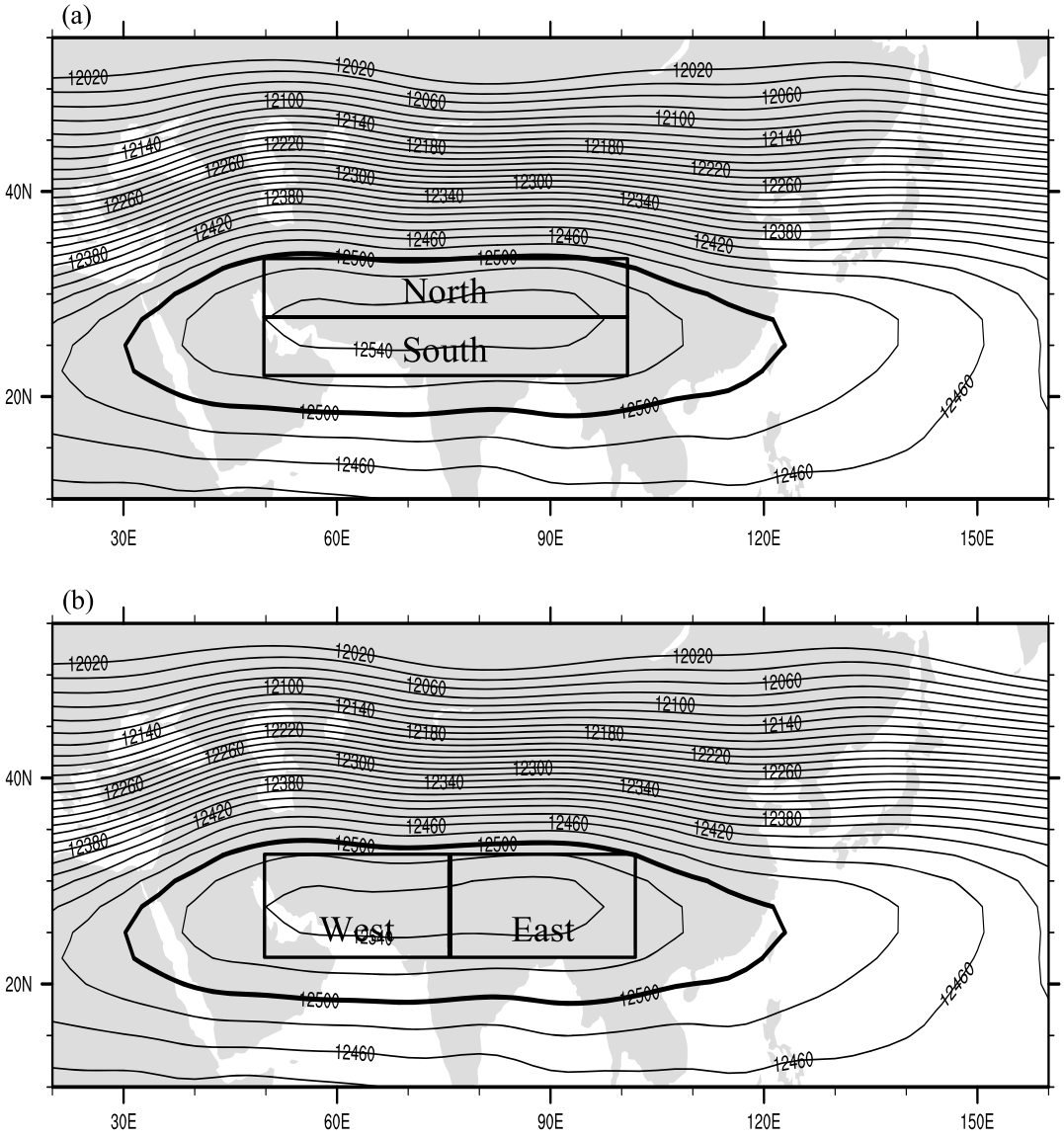

Figure 1. The climatological mean of the 200 hPa geopotential height field and the regions used to define the (a) SAHI-NS index and (b) SAHI-WE index (unit: gpm).

The first principal component of summer extreme precipitation (Figure 2a) is characterized by a tripolar pattern with the major variability locating over the Jiang-Huai River Basin (27.5–33°N, 105–122.5°E) and opposite variability over the northern part (34–40°N, 105–122.5°E) and southern part (20–27.5°N, 105–120°E) of eastern China [*Zhai et al*., 2005]. The years with large extreme precipitation identified in this mode (Figure 2d), i.e., 1980, 1983, 1991, 1996, and 1998, comprise all the years when severe floods occurred over the Jiang-Huai River Basin [*Chang et al*., 2002; *Wang and Zhou*, 2005].

The second principal component (Figures 2b and 2e) shows the interdecadal variability of the summer extreme precipitation over the southern part of eastern China. The results show that there is an interdecadal increase of extreme precipitation over southern China occurring around 1992, which is consistent with previous studies [*Ning and Qian*, 2009; *Chen et al*., 2012; *Li et al*., 2015].

Therefore, three major regions over eastern China (shown as rectangles in Figures 2a–2c) with obvious extreme precipitation variations have been identified through the REOF analysis based on their physical characteristics. The physical boundary between the northern part of eastern China and the Jiang-Huai River Basin is the Huai River, and the physical boundary between the Jiang-Huai River Basin and the

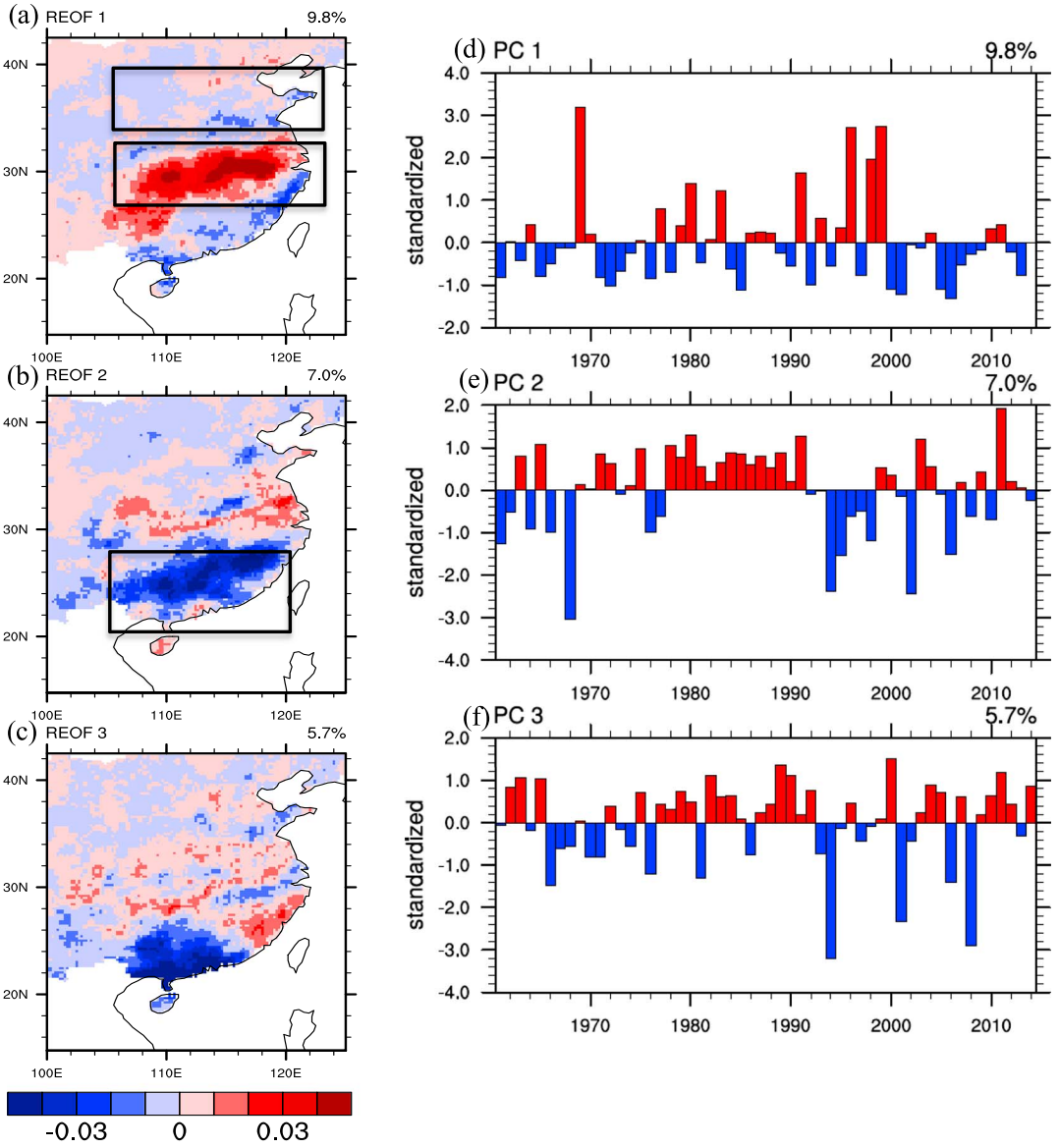

Figure 2. The (a–c) first three REOF spatial patterns and (d–f) corresponding principal components of the summer extreme precipitation over eastern China for the period of 1961–2014. The black rectangles indicate the regions of the northern part of eastern China, Jiang-Huai River Basin, and the southern part of eastern China.

southern part of eastern China is the southern boundary of the Jiang-Huai River basin. These three regions have been used to analyze the influences of SAH on the extreme precipitation over eastern China in the following sections.

Table 1. Correlations Between the SAHI-NS Index, SAHI-WE Index, SAHI-Area Index, and SAHI-mag Index[a]

	SAHI-NS	SAHI-WE	SAHI-area	SAHI-mag
SAHI-NS	1.00	**0.48**	0.09	0.05
SAHI-WE		1.00	−0.05	−0.09
SAHI-area			1.00	**0.95**
SAHI-mag				1.00

[a]Bold type indicates correlations that are significant at the 5% confidence level.

3.2. The Relationships Between the SAH and Extreme Precipitation Over Eastern China

The correlations between the SAHI-NW and the number and amount of the extreme precipitation over the northern part of eastern China are shown in Figures 3a and 3b. Both the number ($r = 0.40$) and amount ($r = 0.37$) of the extreme precipitation

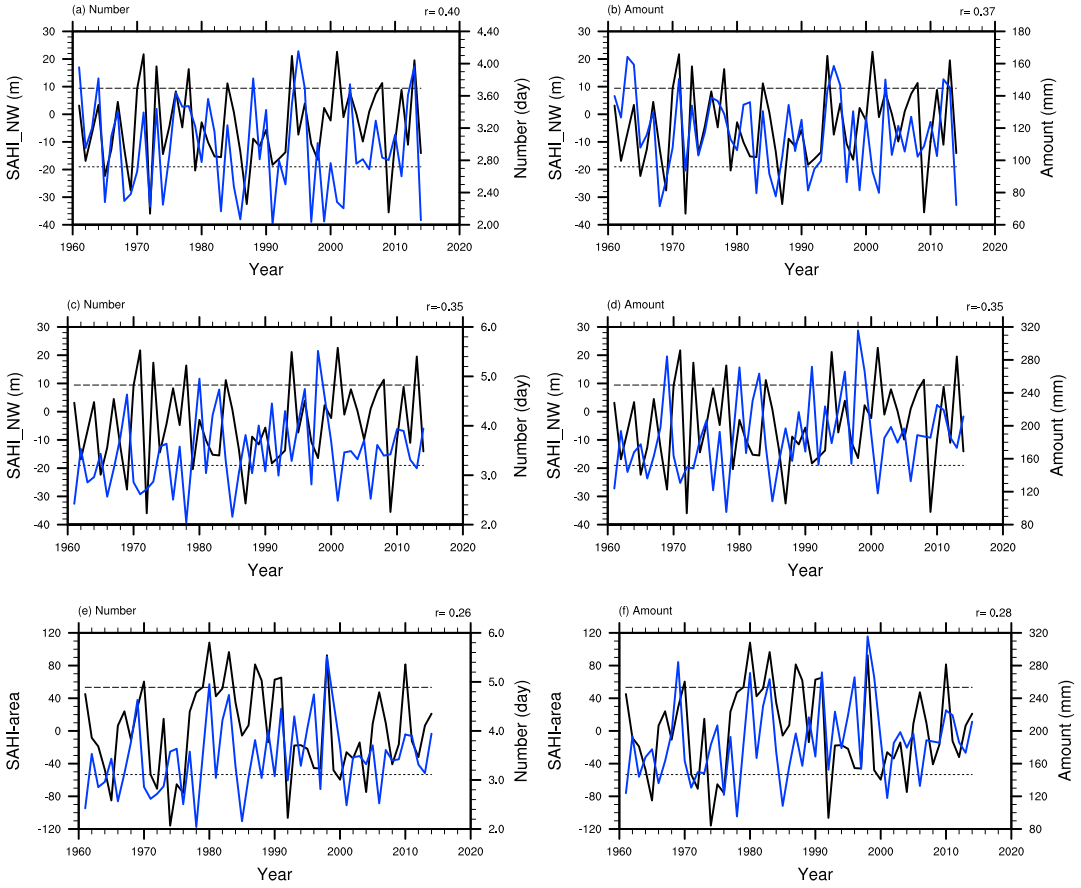

Figure 3. The time series of the SAHI-NW index (black lines) and the (a) number and (b) amount of extreme precipitation over the northern part of eastern China (blue lines), the SAHI-NW index (black lines) and the (c) number and (d) amount of extreme precipitation over the Jiang-Huai River Basin (blue lines), and the detrended SAHI-area index (black lines) and the (e) number and (f) amount of extreme precipitation over the Jiang-Huai River Basin (blue lines). The black dash lines indicate the ±1 standard deviations of the SAH index.

are significantly correlated with SAHI-NW ($p < 0.01$), indicating that when the SAH is located more northwestwardly, there are more extreme precipitation events over the northern part of eastern China. The number ($r = -0.35$) and amount ($r = -0.35$) of the extreme precipitation over the Jiang-Huai River Basin are negatively correlated with the SAHI-NW ($p < 0.05$) (Figures 3c and 3d), indicating that when the SAH is located more northwestwardly, there are fewer extreme precipitation events over the Jiang-Huai River Basin. The number ($r = 0.11$) and amount ($r = 0.16$) of the extreme precipitation over the southern part of eastern China are not significantly correlated with the SAHI-NS ($p > 0.25$), indicating that the northwest movement of the SAH does not influence extreme precipitation over the southern part of eastern China.

Table 2. Correlations Between the SAHI-NW, Detrended SAHI-Area Index, and the Numbers/Amounts of Extreme Precipitation Over the Southern Part of Eastern China, Jiang-Huai River Basin, and the Northern Part of Eastern China[a]

	SAHI-NW	SAHI-area
Northern part	**0.40/0.37**	0.12/0.01
Jiang-Huai River Basin	**−0.35/−0.35**	**0.27/0.29**
Southern part	0.11/0.16	−0.13/−0.13

[a]In each cell, the first correlation coefficient indicates the correlation with the number of extreme precipitation events, and the second correlation coefficient indicates correlation with the amount of extreme precipitation. Bold type indicates correlations are significant at the 5% confidence level.

The SAHI-area index is only significantly correlated with the number ($r = 0.27$) and amount ($r = 0.29$) of the extreme precipitation over the Jiang-Huai River Basin ($p < 0.05$) (Figures 3e and 3f), indicating that when the SAH intensifies and extends to a larger area, it induces more extreme precipitation over the Jiang-Huai River Basin. For here and

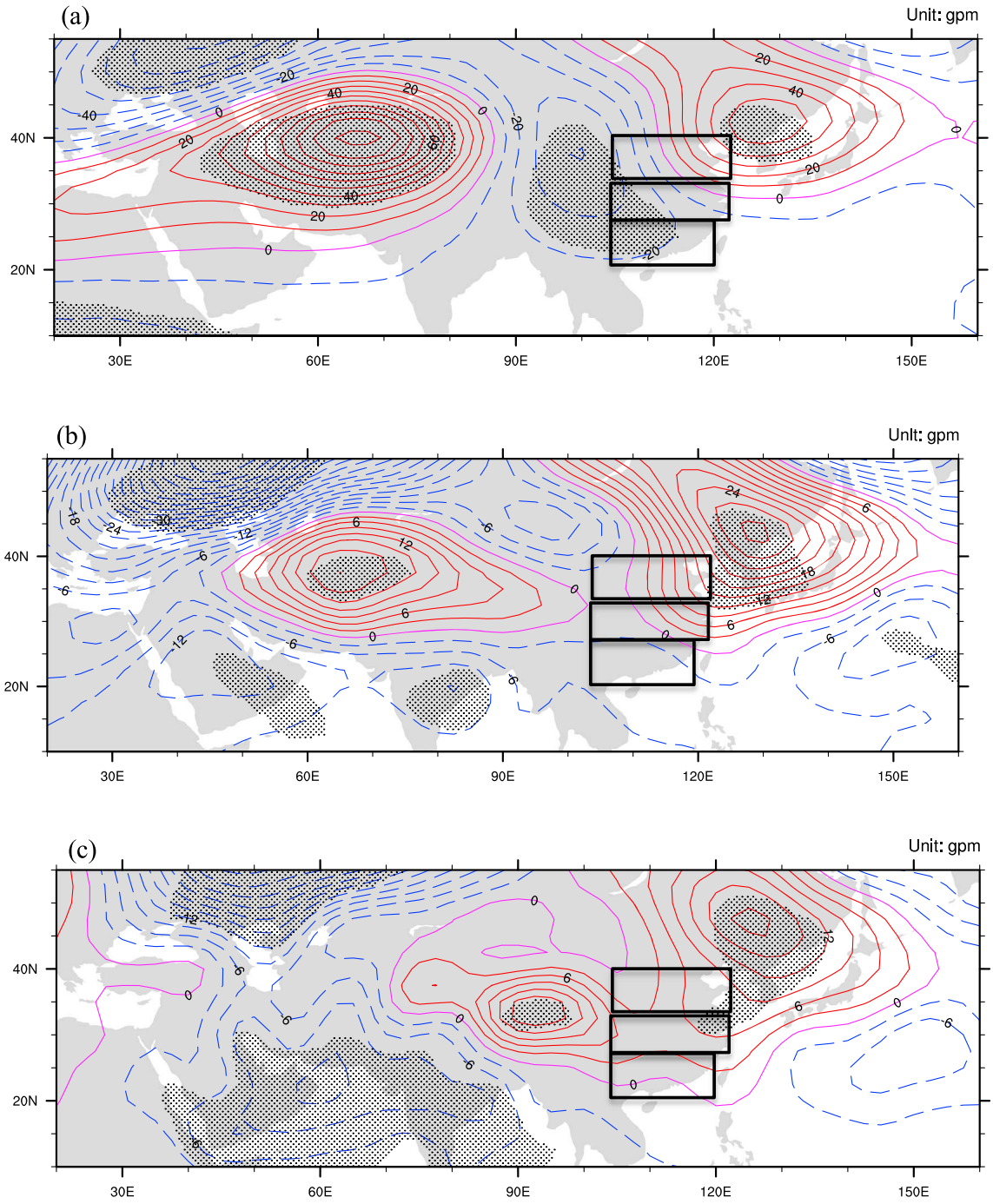

Figure 4. The differences in the (a) 200 hPa geopotential height, (b) 500 hPa geopotential height, (c) 850 hPa geopotential height, (d) 850–500 hPa omega, and (e) low-level moisture flux and corresponding divergence between positive and negative SAHI-NW indices. The stippled areas indicate differences that are significant at the 95% confidence level based on Student's *t* test. The rectangles show the locations of the three characteristic regions of eastern China. Only those moisture flux vectors that are significant at the 90% confidence level are plotted.

the following analysis, since the SAHI-area shows a significant increasing trend, the linear trends of the SAHI-area index and extreme precipitation are removed before the calculation because this study mainly focuses on the interannual influences of the SAH on the extreme precipitation over eastern China. Meanwhile, the number and amount of the extreme precipitation over the northern part ($r = 0.12/0.01$) and the southern part ($r = -0.13/-0.13$) of eastern China are not significantly correlated with the SAHI-area

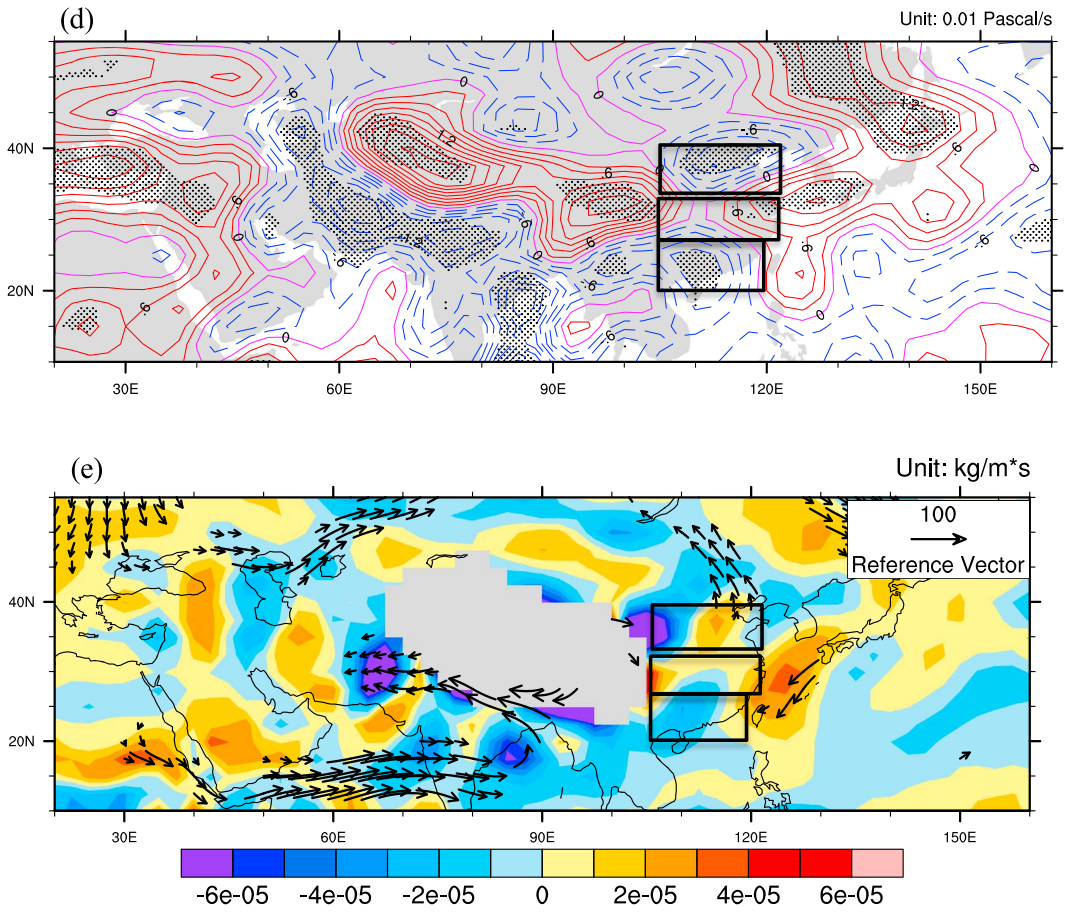

Figure 4. (continued)

index ($p > 0.1$), indicating that the extension and intensification of the SAH does not influence the extreme precipitation over the northern and southern parts of eastern China. The relationships between the two SAH indices and extreme precipitation over the three regions of eastern China are summarized in Table 2.

3.3. Physical Mechanisms Behind the Relationships

Previous studies have shown that because of the nonlinear relationships between the mean climate states and climate extremes, small changes in the mean climate variables (e.g., precipitation) can result in large changes in the frequency and intensity of climate extremes [*Wigley*, 1985; *Wettestein and Mearns*, 2002]. The influences of the SAH on the extreme precipitation over eastern China found in previous sections were also achieved through the changes of the seasonal mean precipitation. Therefore, in this section, the differences of seasonal mean circulation patterns between the years with high and low SAH indices are first compared. Then, the responses of daily precipitation to the mean circulation differences are examined through the changes in the cumulative distribution functions (CDFs).

3.3.1. Differences of the Large-Scale Circulations

To analyze the influence of the SAH on the large-scale circulation patterns, the years with the standardized SAH indices higher than 1 and lower than −1 (cf. Figure 3) were chosen to investigate the differences of the large-scale circulation between years when the SAH is located northwestward and southeastward as well as extends and shrinks.

Between the high and low SAHI-NW years, a difference of 200 hPa geopotential height field over Eurasia shows two positive centers located at (37.5°N, 65°E) and (40°N, 125°E) with magnitudes larger than 50 gpm (Figure 4a), which are north of the climatological location of the SAH (cf. Figure 2). The SAH northwestward

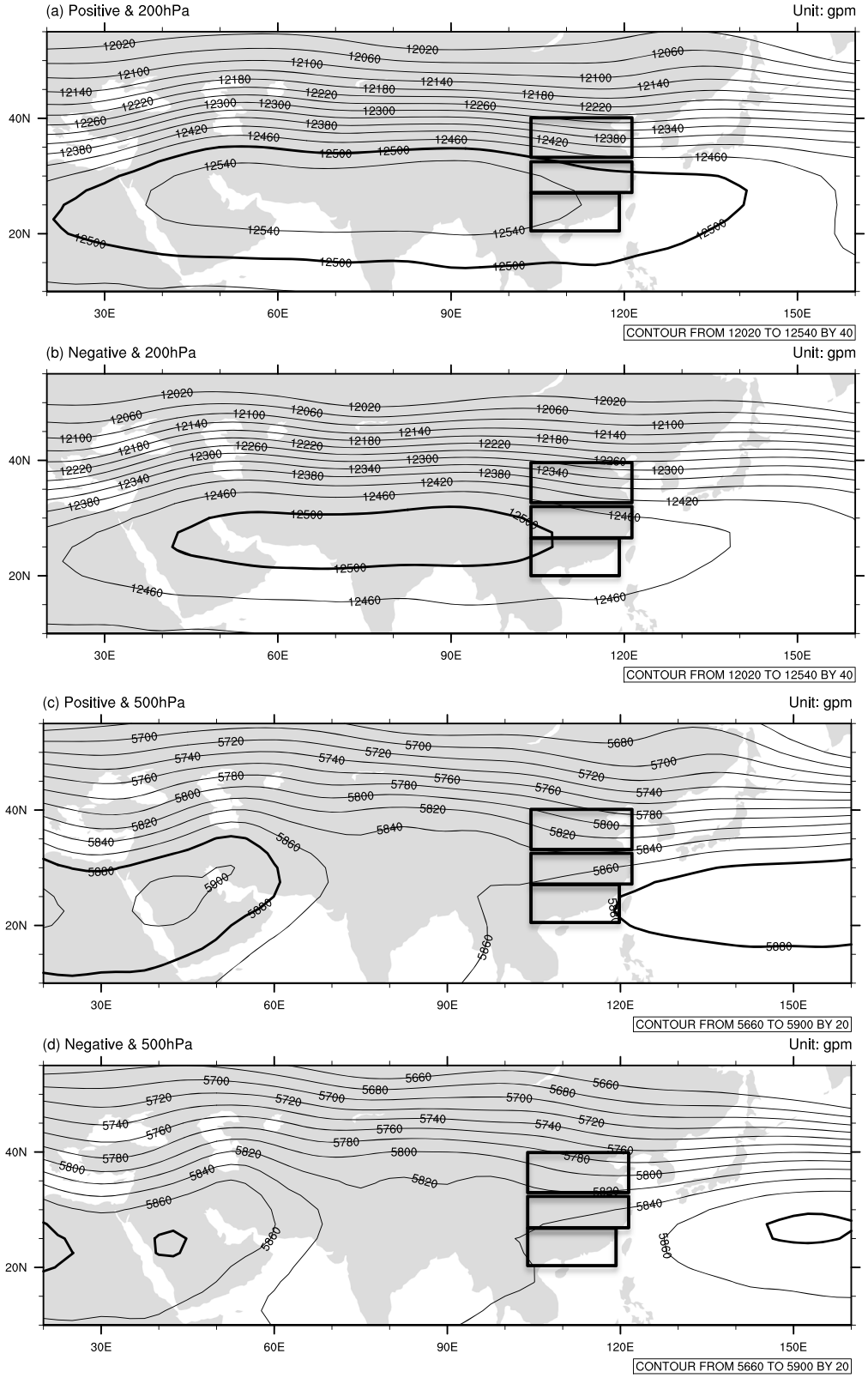

Figure 5. The comparison of (a and b) 200 hPa geopotential height, (c and d) 500 hPa geopotential height, and (e and f) 850 hPa geopotential height and the (g) differences in the 850–500 hPa omega and (h) low-level moisture flux and corresponding divergence between positive and negative SAHI-area indices. The stippled areas indicate differences that are significant at the 95% confidence level based on Student's *t* test. Only those moisture flux vectors that are significant at the 90% confidence level are plotted.

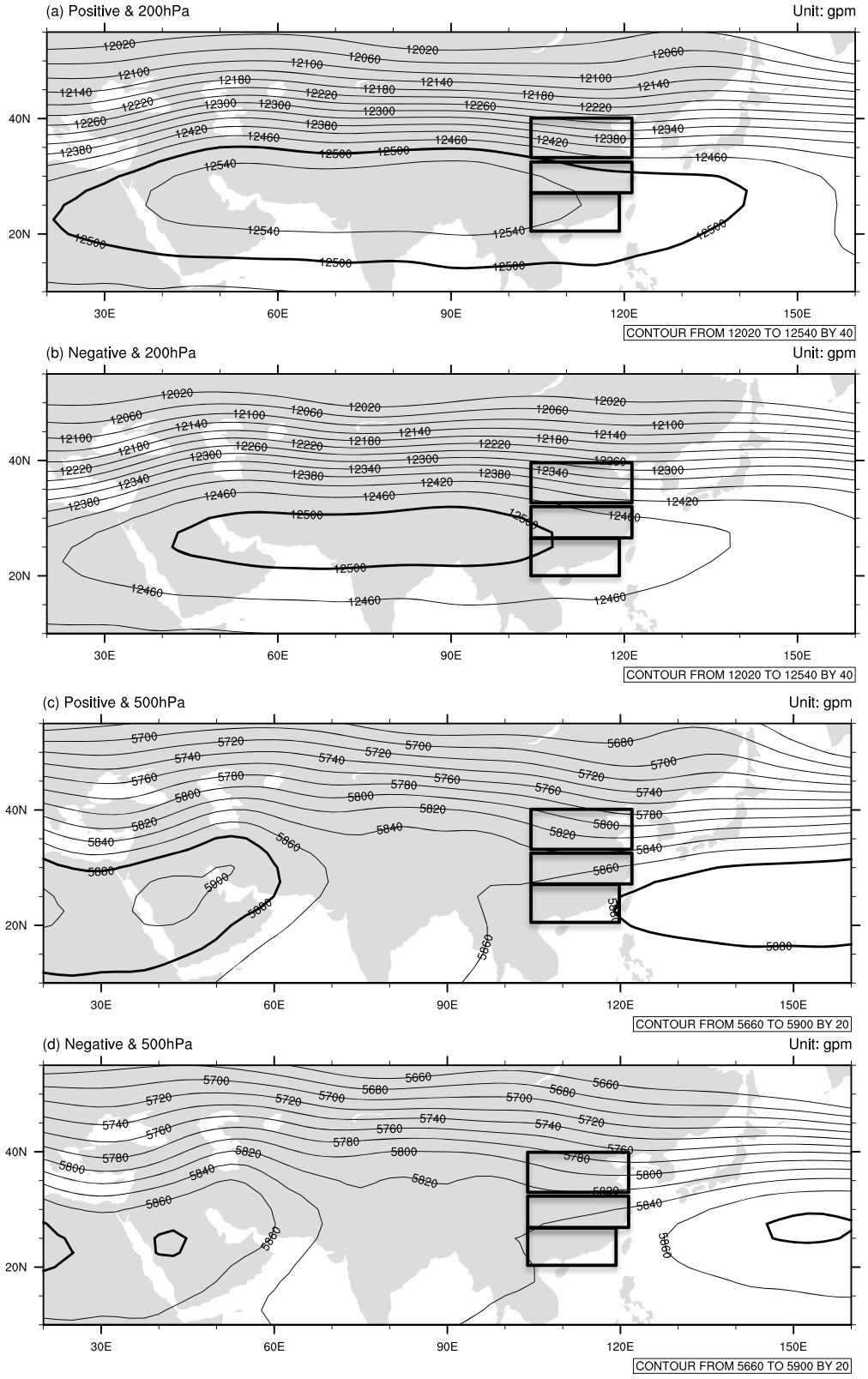

Figure 5. (continued)

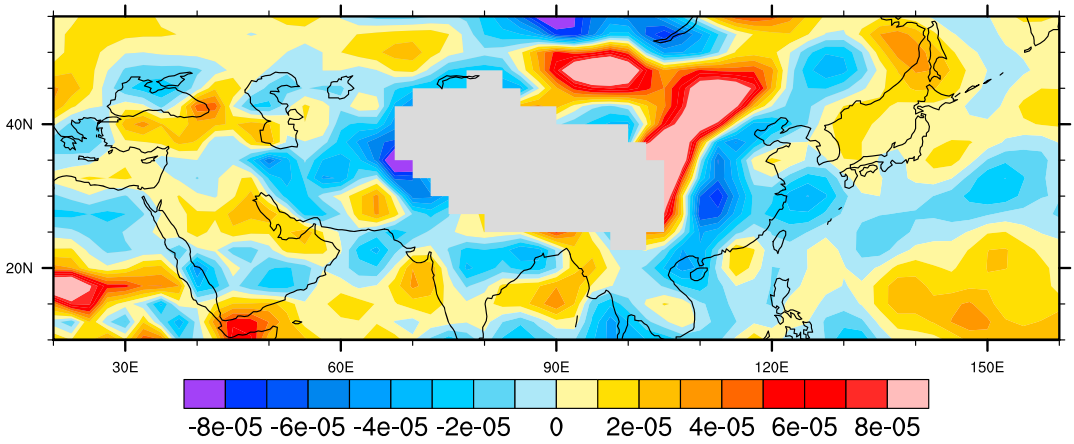

Figure 6. The moisture divergence between the years with moisture supply increases and above average ratios between extreme precipitation and total rainfall and the years with moisture supply increases and below average ratios between extreme precipitation and total rainfall (unit: kg/m^2 S).

shift directly induces the anomalous central Asian high, which then forms the anomalous anticyclonic circulation pattern over northeastern Asia through the propagation of a Rossby wave train along the East Asian jet, as suggested in the mechanism of the Silk Road teleconnection pattern [*Enomoto et al*., 2003; *Ding and Wang*, 2005].

The difference patterns of the middle-level (500 hPa) and low-level (850 hPa) geopotential height fields also show similar patterns with two anticyclones, with the anticyclone over northeastern Asia being more significant (Figures 4b and 4c). This deep barotropic system over northeastern Asia, defined as the Korean High in this study, induces a convergence at its northwestern edge that is located over the northern part of eastern China due to the confluence of the enhanced southerly warm advection and the northerly cold air and a divergence over the region within the system [*Horton*, 2004]. This mechanism is confirmed by the low-level (850–500 hPa) omega difference field, which shows significant negative omega values over the northern part of eastern China and positive omega values over the region extending from Japan to the Jiang-Huai River Basin (Figure 4d). The Korean High also induces an anomalous southeasterly wind, which enhances the water vapor transportation and convergence to the northern part of eastern China (Figure 4e). The combined effect of these aspects induces an increase of precipitation over the northern part of eastern China. Meanwhile, anomalous downward motions (positive omega values) over the Jiang-Huai River Basin (Figure 4d) induce a decrease in precipitation over this region. The magnitudes of the downward velocity over the Jiang-Huai River Basin are lower than the magnitudes of the upward velocity over the northern part of eastern China. Therefore, the correlation coefficients between the SAHI-NW and the extreme precipitation over the northern part of eastern China are higher than those between the SAHI-NS and the extreme precipitation over the Jiang-Huai River Basin (Table 2). The locations of these circulation anomalies also explain why the extreme precipitation over the southern part of eastern China is not significantly influenced by the SAH northwestward shift.

When the SAH extend to larger area, the isoline of 12,500 m extends from 25°E to 135°E (Figure 5a), which is much wider than the negative SAHI-area years (35°E to 110°E) (Figure 5b). The SAH also intensifies with significant positive geopotential height anomalies over almost the entire region at the 200 hPa level. The corresponding positive geopotential height anomalies over the 500 hPa and 850 hPa levels (Figures 5c–5f) indicate the intensification and westward shift of the western Pacific subtropical High (WPSH), shown as the isoline of 5880 m (Figure 5c). As found in previous studies, a stronger SAH is accompanied by a stronger and more extensive WPSH [*Zhang et al*., 2005]. This stronger WPSH suppresses the East Asian Summer Monsoon (EASM) and induces a southward shift of the rain belt to the Jiang-Huai River Basin [*Wang et al*., 2013]. The increasing trend of the SAHI-area (not shown) is also consistent with the westward extension and intensification of the WPSH in recent decades [*Zhou et al*., 2009; *Wang et al*., 2013; *Yun et al*., 2015].

Under this circulation pattern, the Jiang-Huai River Basin is located at the northwestern edge of the WPSH and then experiences the confluence of the southerly moisture transportation due to the WPSH and the

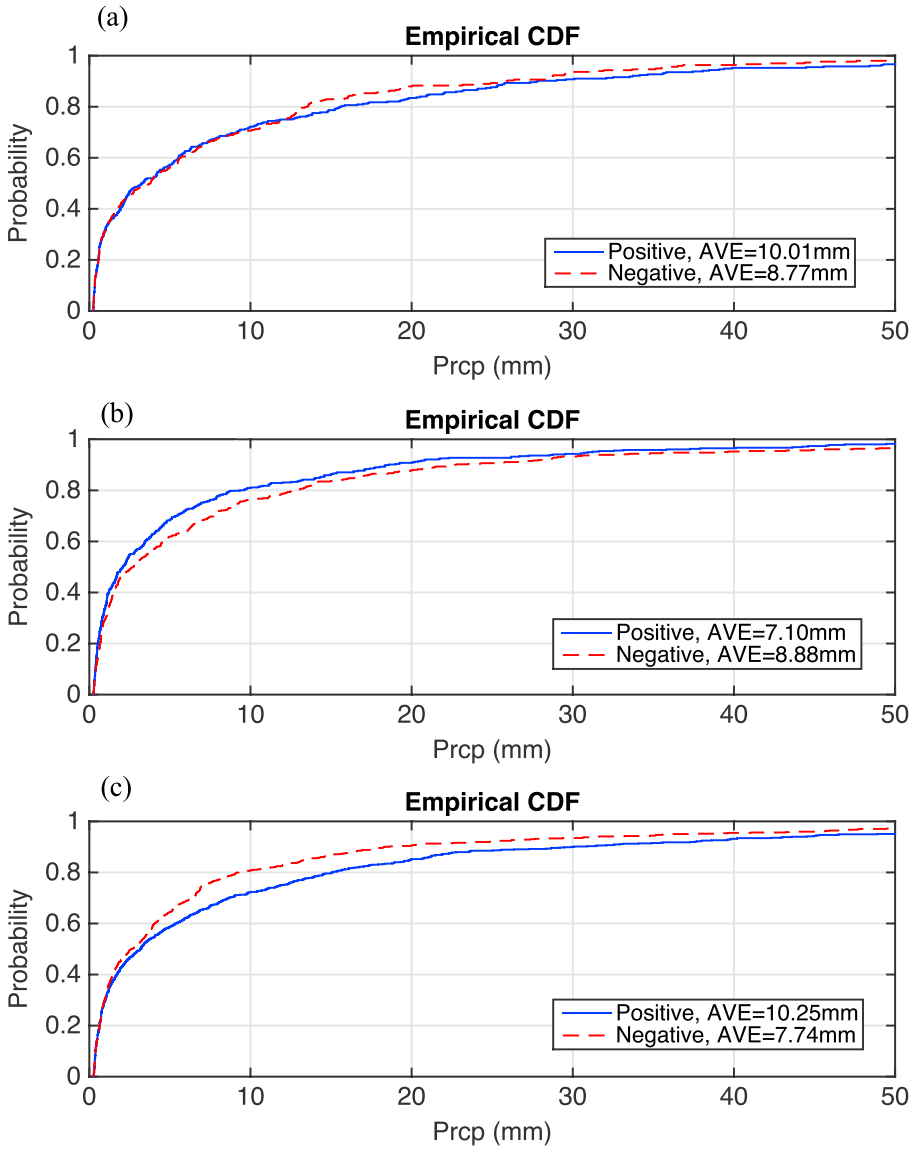

Figure 7. The comparisons of cumulative distributions of the daily precipitation over the typical location of the northern part of eastern China between positive and negative SAHI-NW index values (a), over the typical location of Jiang-Huai River Basin between positive and negative SAHI-NW index values (b), and between positive and negative SAHI-area index values (c).

northerly cold air due to the trough over eastern China (Figures 5e and 5f). The convergence over the Jiang-Huai River Basin is then enhanced (Figure 5g), and more moisture is transported to the Jiang-Huai River Basin (Figure 5h). Therefore, more precipitation, especially convective precipitation, is induced over the Jiang-Huai River Basin [*Wang et al*., 2008] when the SAH intensifies.

To verify the influences of the enhanced moisture supply on the increases of extreme precipitation, the years with a high moisture supply to the Jiang-Huai River Basin (27.5–33°N, 105–122.5°E) (standardized moisture divergence lower than −0.5) and an above average ratio between extreme precipitation and total rainfall and the years with a high moisture supply to the Jiang-Huai River Basin (standardized moisture divergence lower than −0.5) and a below average ratio between extreme precipitation and total rainfall were first selected. Then, the differences of moisture divergence between these two conditions were compared. The results (Figure 6) showed that when the ratio between extreme precipitation and total rainfall is above average, the increase of moisture supply is larger, which is similar to the pattern with high SAHI-area index

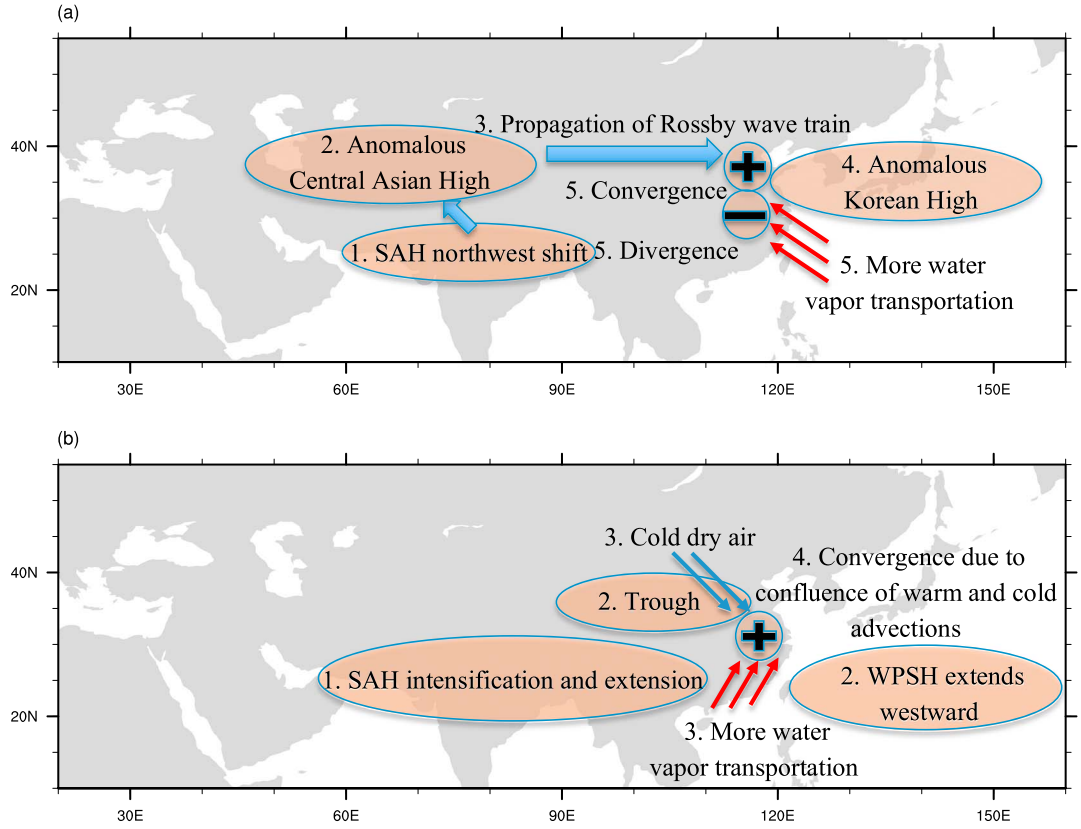

Figure 8. A schematic diagram of the mechanisms that (a) SAH northwestward shift and the (b) intensification and extension influence extreme precipitation over eastern China.

(Figure 5h), indicating that the increase of extreme precipitation is more sensitive to increases of the moisture supply than to the total rainfall.

3.3.2. Responses of the Daily Precipitation

The CDFs of the daily precipitation during the years with high and low SAH indices have been compared to examine the responses of the daily precipitation to the differences of circulation patterns found in the previous section. Because the spatial characteristics of the extreme precipitation over the northern part of eastern China and Jiang-Huai River Basin are fairly homogeneous (Figure 1), two typical locations in the center of the study regions, i.e., (36°N, 120°E) and (30°N, 115°E), were selected to calculate the CDFs of the daily precipitation.

Over the northern part of eastern China, the CDF during high SAHI-NW years shifts to the right side with larger average values (Figure 7a), indicating that there is a greater possibility of extreme precipitation events. Over the Jiang-Huai River Basin, the CDF during high SAHI-NW years shifts to the left side with smaller average values (Figure 7b), indicating a lesser possibility of extreme precipitation events. The influence of the SAHI-area on the CDF over Jiang-Huai River Basin is opposite, with a rightward shift and a larger average value (Figure 7c), indicating a greater possibility of extreme precipitation events. These differences in the CDF values show that the responses of the daily precipitation values to the large-scale circulation patterns lead to a correspondingly greater or lesser possibility of extreme precipitation over eastern China.

4. Conclusions

The different influences of the SAH north-south movement, west-east movement, and area (magnitude) changes in summer extreme precipitation over eastern China, and their corresponding physical mechanisms were systemically investigated after identifying three characteristic regions over eastern

Table 3. Correlations Between the SAHI-NS Index, SAHI-WE Index, Detrended SAHI-Area Index, and the Numbers/Amounts of Extreme Precipitation Over the Northern Part of Eastern China and the Jiang-Huai River Basin With the Niño3.4 Index, AMO Index, and PDO Index[a]

	Niño3.4	AMO	PDO
SAHI-NS	**−0.63**	0.02	**−0.44**
SAHI-WE	**−0.30**	−0.09	−0.05
SAHI-area	0.10	**0.34**	0.22
SAHI-NW	**−0.50**	−0.05	−0.25
Northern part	**−0.32**/**−0.30**	0.11/0.08	−0.08/−0.21
Jiang-Huai River Basin	0.16/0.15	**0.33**/**0.35**	0.25/0.20

[a]Bold type indicates correlations are significant at the 5% confidence level.

China using REOF analysis. The correlations between two SAH indices and extreme precipitation over the three characteristic regions of eastern China show that when the SAH shifts northwestward, there is more extreme precipitation over the northern part of eastern China but less extreme precipitation over the Jiang-Huai River Basin. When the SAH extends to a larger area (and also intensifies), there is more extreme precipitation over the Jiang-Huai River Basin. Meanwhile, the movements and magnitude changes of the SAH have no significant influence on extreme precipitation over the southern part of eastern China.

The analyses of the physical mechanisms reveal that when the SAH shifts northwestward (Figure 8a, feature number 1), it directly causes positive geopotential anomalies over central Asia (Figure 8a, feature number 2). This anomalous central Asian High induces a deep barotropic Korean High (Figure 8a, feature number 4) through the propagation of a Rossby wave train along the East Asian jet (Figure 8a, feature number 3), resulting in two anticyclonic circulations over Eurasia. In a manner that is similar to that of the WPSH, this anomalous Korean High induces an upward movement over the northern part of eastern China that is located at its northwestern edge and a downward movement over the Jiang-Huai River Basin that is located at its southwestern edge. Accompanied by anomalous southeasterly moisture transportation, this circulation pattern induces more extreme precipitation over the northern part of eastern China and less extreme precipitation over the Jiang-Huai River Basin (Figure 8a, feature number 5). When the SAH intensifies and extends to a larger area (Figure 8b, feature number 1), the WPSH also intensifies and stretches westward (Figure 8b, feature number 2), so that the EASM is suppressed and the rain belt shifts southward. The Jiang-Huai River Basin located at the northwestern edge of the WPSH experiences more convergence (Figure 8b, feature number 4) resulting from the confluence of moist warm advection due the WPSH and cold dry advection due to the trough (Figure 8b, feature number 3) and then more extreme precipitation. The daily precipitation responds to the changes of the seasonal mean circulation that favors more extreme precipitation with CDF shifts toward the right side, resulting in a greater probability of extreme precipitation defined at the tails of the CDFs and vice versa. These mechanisms are summarized in Figure 8.

These influences and the corresponding physical mechanisms found in this study contribute to a better understanding of the variability of extreme precipitation over eastern China. These findings can also help improve future projections of regional extreme precipitation and help decision makers prepare adaptations with respect to future climate changes and corresponding mitigation strategies.

In addition to the relationships between extreme precipitation over eastern China and the SAH found in this study, both the extreme precipitation over eastern China and the SAH have significant correlations with the Atlantic Multidecadal Oscillation (AMO), Niño3.4, and Pacific Decadal Oscillation (PDO) indices (Table 3), indicating that large-scale modes of climate variability may drive the changes of both the SAH and regional extreme precipitation. Therefore, the SAH may be a bridge that transfers the influences of large-scale modes of climate variability to the regional extreme precipitation. The potential mechanisms that the large-scale modes of climate variability impact the movements and intensity of the SAH may be achieved through the South Asian Monsoon intensity changes and precipitation changes over northern India, which influence the intensity of the central Asian high. The corresponding mechanisms behind these relationships will be investigated in a future study.

Acknowledgments
This research has been jointly supported by the National Natural Science Foundation of China (grant 41501210), the National Key Research and Development Program of China (grant 2016YFA0600401), the National Natural Science Foundation of China (grants 41420104002 and 41371209), the Jiangsu Province Natural Science Foundation (grant BK20150977), and the Priority Academic Development Program of Jiangsu Higher Education Institutions (grant 164320H116). We want to thank Raymond S. Bradley for fruitful discussions. Jia Wu (wujia@cma.gov.cn) from the National Climate Center, China Meteorological Administration, kindly provided the high-resolution observation data (CN05.1 data). More details about this data can be found at *Wu and Gao* [2013]. The Niño3.4, AMO, and PDO indices and the NCEP Reanalysis data were provided by the NOAA/OAR/ESRL PSD, Boulder, Colorado, USA, from their website at http://www.esrl.noaa.gov/psd/.

References

Alexander, L. V., et al. (2006), Global observed changes in daily climate extremes of temperature and precipitation, *J. Geophys. Res.*, *111*, D05109, doi:10.1029/2005JD006290.
Barnston, A. G., and R. E. Livezey (1987), Classification, seasonality, and persistence of low-frequency atmospheric circulation patterns, *Mon. Weather Rev.*, *115*, 1083–1126.
Bradbury, B., D. Keim, and C. P. Wake (2003), The influence of regional storm tracking and teleconnections on winter precipitation in the Northeastern United States, *Ann. Assoc. Am. Geogr.*, *93*, 544–556.
Brown, S. J., J. Caesar, and C. A. T. Ferro (2008), Global changes in extreme daily temperature since 1950, *J. Geophys. Res.*, *113*, D05115, doi:10.1029/2006JD008091.
Chang, C.-P., G. Wu, B. Jou, and C.-Y. Lam (2002), *East Asia and Western Pacific Meteorology and Climate: Selected Papers of the Fourth Conference*, World Sci. Co. Pte. Ltd., Singapore.
Chen, G., and R. Huang (2012), Excitation mechanisms of the teleconnection patterns affecting the July precipitation in northwest China, *J. Clim.*, *25*, 7834–7851.
Chen, J., R. Wu, and Z. Wen (2012), Contribution of South China Sea tropical cyclones to an increase in southern China summer rainfall around 1993, *Adv. Atmos. Sci.*, *29*, 585–598.
Chen, S., W. Chen, and K. Wei (2013), Recent trends in winter temperature extremes in eastern China and their relationship with the Arctic Oscillation and ENSO, *Adv. Atmos. Sci.*, *30*, 1712–1724.
Coffel, E. D., and R. M. Horton (2015), Climate change and the impact of extreme temperature on aviation, *Weather Clim. Soc.*, *7*, 94–101.
Coleman, J. S., and J. C. Rogers (2003), Ohio River Valley winter moisture conditions associated with the Pacific-North American teleconnection pattern, *J. Clim.*, *16*, 969–981.
Ding, Q., and B. Wang (2005), Circumglobal teleconnection in the Northern Hemisphere summer, *J. Clim.*, *18*, 3483–3505.
Dominguez, F., and P. Kumar (2005), Dominant modes of moisture flux anomalies over North America, *J. Hydrometeorol.*, *6*, 194–209.
Dommenget, D., and M. Latif (2002), A cautionary note on the interpretation of EOFs, *J. Clim.*, *15*, 216–225.
Donat, M. G., et al. (2013), Updated analyses of temperature and precipitation extremes indices since the beginning of the twentieth century: The HadEX2 dataset, *J. Geophys. Res. Atmos.*, *118*, 2098–2118, doi:10.1002/jgrd.50150.
Easterling, D. R., J. L. Evans, P. Y. Groisman, T. R. Karl, K. E. Kunkel, and P. Ambenje (2000a), Observed variability and trends in extreme climate events: A brief review, *Bull. Am. Meteorol. Soc.*, *81*, 417–425.
Easterling, D. R., G. A. Meehl, C. Parmesan, S. A. Changnon, T. R. Karl, and L. O. Mearns (2000b), Climate extremes: Observations, modeling, and impacts, *Science*, *289*, 2068–2074.
Enomoto, T., B. J. Hoskins, and Y. Matsuda (2003), The formation mechanism of the Bonin high in August, *Q. J. R Meteorol. Soc.*, *129*, 157–178.
Frich, P., L. V. Alexander, P. Della-Marta, B. Gleason, and M. Haylock (2002), Observed coherent changes in climatic extremes during the second half of the twentieth century, *Clim. Res.*, *19*, 193–212.
Ge, Y., G. Gong, and A. Frei (2009), Physical mechanism linking the winter Pacific-North American teleconnection pattern to spring North America snow depth, *J. Clim.*, *22*, 5135–5148.
Griffths, M. L., and R. S. Bradley (2007), Variations of twentieth-century temperature and precipitation extreme indicators in the northeast United States, *J. Clim.*, *20*, 5401–5417.
Hannachi, A. (2007), Pattern hunting in climate: A new method for finding trends in gridded climate data, *Int. J. Climatol.*, *27*, 1–15.
Hannachi, A., I. Jolliffe, and D. Stephenson (2007), Empirical orthogonal functions and related techniques in atmospheric science: A review, *Int. J. Climatol.*, *27*, 1119–1152.
Hartley, S., and M. J. Keables (1998), Synoptic associations of winter climate and snowfall variability in New England, USA, 1950–1992, *Int. J. Climatol.*, *18*, 281–298.
Hartmann, D. L., et al. (2013), Observations: atmosphere and surface, in *Climate Change 2013: The Physical Science Basis. Contribution of Working Group I to the Fifth Assessment Report of the Intergovernmental Panel on Climate Change*, edited by T. F. Stocker et al., Cambridge Univ. Press, Cambridge.
Horton, J. R. (2004), *An Introduction to Dynamic Meteorology*, 4th ed., Elsevier Acad. Press, Amsterdam.
Horton, R., E. D. Coffel, J. M. Winter, and D. A. Bader (2015), Projected changes in extreme temperature events based on the NARCCAP model suite, *Geophys. Res. Lett.*, *18*, 7722–7731, doi:10.1002/2015GL064914.
Huang, R., Y. Liu, and T. Feng (2013), Interdecadal change of summer precipitation over Eastern China around the late-1990s and associated circulation anomalies, internal dynamical causes, *Chin. Sci. Bull.*, *58*, 1339–1349, doi:10.1007/s11434-012-5545-9.
Jiang, X., Y. Li, S. Yang, and R. Wu (2011), Interannual and interdecadal variations of the South Asian and western Pacific subtropical highs and their relationships with Asian-Pacific summer climate, *Meteorol. Atmos. Phys.*, *113*, 171–180.
Joyce, T. M. (2002), One hundred plus years of wintertime climate variability in the eastern United States, *J. Clim.*, *15*, 1076–1086.
Kalnay, E., et al. (1996), The NCEP/NCAR 40-year reanalysis project, *Bull. Am. Meteorol. Soc.*, *77*, 437–470.
Kunkel, K. E., and J. R. Angel (1999), Relationship of ENSO to snowfall and related cyclone activity in the contiguous United States, *J. Geophys. Res.*, *104*(D16), 19,425–19,434, doi:10.1029/1999JD900010.
Leathers, D. J., B. Yarnal, and M. A. Palecki (1991), The Pacific/North American Teleconnection Pattern and United States climate. Part I: Regional temperature and precipitation associations, *J. Clim.*, *4*, 517–528.
Li, H., H. Chen, and H. Wang (2015), Changes in clustered extreme precipitation events in south China and associated atmospheric circulations, *Int. J. Climatol.*, *171*, 334–339.
Li, T., R. M. Horton, and P. L. Kinney (2013), Projections of seasonal patterns in temperature-related deaths for Manhattan, New York, *Nat. Clim. Change*, *3*, 717–721.
Li, W., P. Zhai, and J. Cai (2011), Research on the relationship of ENSO and the frequency of extreme precipitation events in China, *Adv. Clim. Change Res.*, *2*, 101–107.
Lian, T., and D. Chen (2012), An evaluation of rotated EOF analysis and its application to tropical Pacific SST variability, *J. Clim.*, *25*, 5361–5373.
Liang, Y.-C., M.-H. Lo, and J.-Y. Yu (2014), Asymmetric responses of land hydroclimatology to two types of El Niño in the Mississippi River Basin, *Geophys. Res. Lett.*, *41*, 582–588, doi:10.1002/2013GL058828.
Liu, B., G. Wu, J. Mao, and J. He (2013), Genesis of the South Asian High and its impact on the Asian summer monsoon onset, *J. Clim.*, *26*, 2976–2991.
Loikith, P. C., and A. J. Broccoli (2014a), Comparison between observed and model simulated atmospheric circulation patterns associated with extreme temperature days over North America using CMIP5 historical simulations, *J. Clim.*, *28*, 2063–2079.

Loikith, P. C., and A. J. Broccoli (2014b), The influence of recurrent modes of climate variability on the occurrence of winter and summer extreme temperatures over North America, *J. Clim.*, *27*, 1600–1618.
Mao, R., D.-Y. Gong, J. Yang, and J.-D. Bao (2011), Linkage between the Arctic Oscillation and winter extreme precipitation over central-southern China, *Clim. Res.*, *50*, 187–2011.
Mason, R. B., and C. Anderson (1958), The development and decay of the 100 mb summertime anticyclone over southern Asia, *Mon. Weather Rev.*, *91*, 3–12.
Meehl, G. A., and C. Tebaldi (2004), More intense, more frequent, and longer lasting heat waves in the 21st century, *Science*, *305*, 994–997.
Meehl, G. A., et al. (2007), Global climate projections, in *Climate Change 2007: The Physical Science Basis*, edited by S. Solomon et al., pp. 747–845, Cambridge Univ. Press, Cambridge, U. K., and New York.
Ning, L., and R. S. Bradley (2014), Winter precipitation variability and corresponding teleconnections over the northeastern United States, *J. Geophys. Res. Atmos.*, *119*, 7931–7945, doi:10.1002/2014JD021591.
Ning, L., and R. S. Bradley (2015a), Winter climate extremes over the northeastern United States and southeastern Canada and teleconnections with large-scale modes of climate variability, *J. Clim.*, *28*, 3289–3310, doi:10.1175/JCLI-D-13-00750.1.
Ning, L., and R. S. Bradley (2015b), Influence of Eastern Pacific and Central Pacific El Niño events on winter climate extremes over the eastern and central United States, *Int. J. Climatol.*, *35*, 4756–4770, doi:10.1002/joc.4321.
Ning, L., and R. S. Bradley (2016), NAO and PNA influences on winter temperature and precipitation over the eastern United States in CMIP5 GCMs, *Clim. Dyn.*, *46*, 1257–1276, doi:10.1007/s00382-015-2643-9.
Ning, L., and Y. Qian (2009), Interdecadal change of extreme precipitation over South China and its mechanism, *Adv. Atmos. Sci.*, *26*, 109–118.
Ning, L., M. E. Mann, R. Crane, and T. Wagener (2012a), Probabilistic projections of climate change for the mid-Atlantic region of the United States—Validation of precipitation downscaling during the historical era, *J. Clim.*, *25*, 509–526.
Ning, L., M. E. Mann, R. Crane, T. Wagener, R. G. Najjar Jr., and R. Singh (2012b), Probabilistic projections of anthropogenic climate change impacts on precipitation for the mid-Atlantic region of the United States, *J. Clim.*, *25*, 5273–5291.
Ning, L., E. E. Riddle, and R. S. Bradley (2015), Projected changes in climate extremes over the northeastern United States, *J. Clim.*, *18*, 2475–2493, doi:10.1175/JCLI-D-14-00150.1.
Qian, Y., Q. Zhang, Y. Yao, and X. Zhang (2002), Seasonal variation and heat preference of the South Asia High, *Adv. Atmos. Sci.*, *19*, 821–836.
Rasmusson, E. M., and J. M. Wallace (1983), Meteorological aspects of the El Niño/Southern Oscillation, *Science*, *222*, 1195–1202.
Ren, G., H. Wu, and Z. Chen (2000), Spatial patterns of change trend in rainfall of China [in Chinese], *Quart. J. Appl. Meteorol.*, *11*, 322–330.
Ropelewski, C. F., and M. S. Halpert (1986), North American precipitation and temperature patterns associated with the El Niño/Southern Oscillation (ENSO), *Mon. Weather Rev.*, *114*, 2352–2361.
Sillmann, J., V. V. Kharin, X. Zhang, F. W. Zwiers, and D. Bronaugh (2013a), Climate extremes indices in the CMIP5 multimodel ensemble: Part 1. Model evaluation in the present climate, *J. Geophys. Res. Atmos.*, *118*, 1716–1733, doi:10.1002/jgrd.50203.
Sillmann, J., V. V. Kharin, F. W. Zwiers, X. Zhang, and D. Bronaugh (2013b), Climate extremes indices in the CMIP5 multimodel ensemble: Part 2. Future climate projections, *J. Geophys. Res. Atmos.*, *118*, 2473–2493, doi:10.1002/jgrd.50188.
Trenberth, K. E. (1997), The definition of El Niño, *Bull. Am. Meteorol. Soc.*, *78*, 2771–2777.
Wallace, J. M., and D. S. Gutzler (1981), Teleconnections in the geopotential height field during the Northern Hemisphere winter, *Mon. Weather Rev.*, *109*, 784–812.
Wang, B., Z. Wu, J. Li, J. Liu, C.-P. Chang, Y. Ding, and G. Wu (2008), How to measure the strength of the East Asian Summer Monsoon, *J. Clim.*, *21*, 4449–4463.
Wang, B., B. Xiang, and J.-Y. Lee (2013), Subtropical High predictability establishes a promising way for monsoon and tropical storm predictions, *Proc. Natl. Acad. Sci. U.S.A.*, *110*, 2718–2722.
Wang, F., S. Yang, W. Higgins, Q. Li, and Z. Zuo (2014), Long-term changes in total and extreme precipitation over China and the United States and their links to oceanic-atmospheric features, *Int. J. Climatol.*, *34*, 286–302.
Wang, H., and S. He (2015), The North China/Northeastern Asia severe summer drought in 2014, *J. Clim.*, *28*, 6667–6681.
Wang, Y., and L. Zhou (2005), Observed trends in extreme precipitation events in China during 1961–2001 and the associated changes in large-scale circulation, *Geophys. Res. Lett.*, *32*, L09707, doi:10.1029/2005GL022574.
Wei, W., R. Zhang, and M. Wen (2012), Meridional variation of South Asia High and its relationship with the summer precipitation over China (in Chinese), *J. Appl. Meteorol. Sci.*, *23*, 650–659.
Wei, W., R. Zhang, M. Wen, X. Rong, and T. Li (2014), Impact of Indian summer monsoon on the South Asian High and its influence on summer rainfall over China, *Clim. Dyn.*, *43*, 1257–1269.
Wei, W., R. Zhang, M. Wen, B.-J. Kim, and J.-C. Nam (2015), Interannual variation of the South Asian High and its relation with Indian and East Asian summer monsoon rainfall, *J. Clim.*, *28*, 2623–2634.
Wettestein, J. J., and L. O. Mearns (2002), The influence of North Atlantic-Arctic Oscillation on mean, variance, and extremes of temperature in the northeastern United States and Canada, *J. Clim.*, *15*, 3586–3600.
Wigley, T. (1985), Impact of extreme events, *Nature*, *316*, 106–107.
Wilks, D. S. (2006), *Statistical Methods in Atmospheric Sciences*, 2nd ed., 648 pp., Academic Press, Burlington, Mass.
Wu, A., W. W. Hsieh, and A. Shabbar (2005), The nonlinear patterns of North American winter temperature and precipitation associated with ENSO, *J. Clim.*, *18*, 1736–1752.
Wu, J., and X. J. Gao (2013), A gridded daily observation dataset over China region and comparison with the other datasets [in Chinese with English abstract], *Chin. J. Geophys.*, *56*, 1102–1111, doi:10.6038/g20130406.
Xu, Y., X. Gao, Y. Shen, C. Xu, Y. Shi, and F. Giorgi (2009), A daily temperature dataset over China and its application in validating a RCM simulation, *Adv. Atmos. Sci.*, *26*, 763–772.
You, Q., et al. (2011), Changes in daily climate extremes in China and their connection to the large scale atmospheric circulation during 1961–2003, *Clim. Dyn.*, *36*, 2399, doi:10.1007/s00382-009-0735-0.
Yu, J.-Y., Y. Zou, S. T. Kim, and T. Lee (2012), The changing impact of El Niño on US winter temperatures, *Geophys. Res. Lett.*, *39*, L15702, doi:10.1029/2012GL052483.
Yun, K.-S., K.-J. Ha, S.-W. Yeh, B. Wang, and B. Xiang (2015), Critical role of boreal summer North Pacific subtropical highs in ENSO transition, *Clim. Dyn.*, *44*, 1979, doi:10.1007/s00382-014-2193-6.
Zhai, P., A. Sun, F. Ren, X. Liu, B. Gao, and Q. Zhang (1999), Changes of climate extremes in China, *Clim. Change*, *42*, 203–218.
Zhai, P., X. Zhang, H. Wan, and X. Pan (2005), Trends in total precipitation and frequency of daily precipitation extremes over China, *J. Clim.*, *18*, 1096–1108.
Zhang, L., and T. Zhou (2015), Drought over East Asia: A review, *J. Clim.*, *28*, 3375–3399.

Zhang, P., S. Yang, and V. E. Kousky (2005), South Asian High and Asian-Pacific-American climate teleconnection, *Adv. Atmos. Sci.*, *22*, 915–923.
Zhang, P., Y. Liu, and B. He (2016), Impact of East Asian summer monsoon heating on the interannual variation of the South Asian High, *J. Clim.*, *29*, 159–173.
Zhang, Q., and Y. Qian (2000), Interannual and Interdecadal variations of the South Asia High (in Chinese), *Chin. J. Atmos. Sci.*, *24*, 67–78.
Zhang, Q., G. Wu, and Y. Qian (2002), The bimodality of the 100 hPa South Asia High and its relationship to the climate anomaly over East Asia in summer, *J. Meteorol. Soc. Jpn.*, *80*, 733–744.
Zhang, R. (2015), Changes in East Asian summer monsoon and summer rainfall over eastern China during recent decades, *Sci. Bull.*, *60*, 1222–1224.
Zhou, T., et al. (2009), Why the western Pacific subtropical High has extended westward since the late 1970s, *J. Clim.*, *22*, 2199–2215.